



Determination of the interfacial heat transfer coefficient between forced air and sand at Reynold's numbers relevant to smouldering combustion



Marco A.B. Zanoni^a, José L. Torero^b, Jason I. Gerhard^{a,*}

^a Department of Civil and Environmental Engineering, University of Western Ontario, London, Ontario N6A 5B9, Canada

^b School of Civil Engineering, University of Queensland, St. Lucia Campus, Brisbane 4067, Australia

ARTICLE INFO

Article history:

Received 23 March 2017

Received in revised form 5 June 2017

Accepted 8 June 2017

Keywords:

Smouldering

Porous medium

Heat loss

Inverse modelling

Local thermal non-equilibrium

Interfacial heat transfer coefficient

ABSTRACT

Heat transfer between flowing air and a fixed sand bed at low Reynold's number (i.e., $Re < 30$) is central to numerous natural and applied processes, including smouldering combustion. The most widely used correlation for the heat transfer coefficient (h_{sg}) predicts Nusselt numbers so high, it effectively presumes local thermal equilibrium for these systems; **an assumption that has never been tested**. In this work, twelve column experiments combined with numerical modelling quantify h_{sg} across a range of relevant sand grain sizes ($0.125 < d_p < 2.000$ mm) and air flow rates ($0.5 < Re < 31$). All of the sand properties were determined independently, with only h_{sg} determined via inverse modelling. A new empirical correlation for h_{sg} is obtained, $Nu = 0.001 (Re^{1.97} Pr^{1/3})$, which is then validated against two additional experiments. A newly developed criterion for assuming local thermal equilibrium is shown to be violated in all of these convection-dominated experiments and the extent of non-equilibrium between sand and air is quantified. **The centerline temperatures are demonstrated to be sensitive not only to h_{sg} but also to a global heat loss coefficient quantified from the experiments in a novel manner**. Overall, the new h_{sg} correlation is demonstrated to be reliable for predicting the interphase heat transfer in these systems and its application is expected to be valuable for a wide range of processes including smouldering.

© 2017 Elsevier Ltd. All rights reserved.

1. Introduction

Smouldering is defined as an oxygen-limited, flameless form of combustion with low temperatures and slow propagation rates relative to flaming [1]. It is a heterogeneous, exothermic chemical reaction between the (solid or liquid) reactive fuel and oxygen, using the heat released during the exothermic process to sustain the combustion front [1–4]. Traditionally, research on smouldering focused on porous organic solids, such as polyurethane foam and peat in the context of fire safety [5]. Examples include smouldering involved in residential, industrial, and forest fires and subsurface fires in coal seams.

Recently, smouldering has been developed as an engineering technology. Applications include liberating oil from shale [6–8], treating human feces [9], underground coal gasification [10], tire recycling [11], treating wastewater biosolids [12], and remediating contaminated soil [13–16]. In each case, smouldering is enabled by

the fact that the organic fuels are embedded in an inert porous matrix (e.g., rock, soil, sand). This matrix plays important roles, including: (i) its permeability permits oxygen transfer to the reaction zone by convection and diffusion [1,4,15,17], and (ii) **its high heat capacity acts as a thermal reservoir, which recycles the released energy into the reaction. This energy efficiency enables the smouldering of fuels with low calorific values** [18–20].

Generally, predictions of smouldering must take into account the transport of momentum, mass, and energy in the solid and fluid phases [21,22]. The transport of energy is dependent on the ability of the porous medium to store, conduct, and radiate heat, as well as convective transfer between phases. Modelling of energy generally follows one of two approaches: Local Thermal Equilibrium (LTE) or Local Thermal Non-Equilibrium (LTNE) [23–28]. In LTE, the local temperature of the solid and gas phases is assumed to be the same so only one energy equation is employed. In LTNE, this is not assumed, so the energy equation for each phase is solved:

$$(1 - \phi)(\rho_s C_{ps}) \frac{\partial T_s}{\partial t} = (1 - \phi) \frac{\partial}{\partial x} \left((k_s + k_{rad}) \frac{\partial T_s}{\partial x} \right) - U \left(\frac{A_{s,c}}{V_c} \right) (T_s - T_\infty) + h_{sg} \left(\frac{A_{s,sp}}{V_{sp}} \right) (T_g - T_s) \quad (1)$$

* Corresponding author at: Department of Civil and Environmental Engineering, The University of Western Ontario, Spencer Engineering Building, Rm. 3029, London, Ontario N6A 5B9, Canada.

E-mail addresses: mbazelat@uwo.ca (M.A.B. Zanoni), j.torero@uwo.ca (J.L. Torero), jgerhard@uwo.ca (J.I. Gerhard).

Nomenclature

Abbreviations

DSC	Differential Scanning Calorimetry
LM	Levenberg-Marquardt
LTE	Local Thermal Equilibrium
LTNE	Local Thermal Non-Equilibrium
NRMSD	Normalized Root-Mean-Square Deviation
REV	Representative Elementary Volume

Latin letters

a_v	surface area per unit volume, m^{-1}
A	cross-sectional area, m^2
A_s	surface area, m^2
Bi	biot number
C_p	specific heat capacity, $\text{J kg}^{-1} \text{K}^{-1}$
D	diameter of the column, m
d_p	particle diameter, m
E	energy, J
g	gravitational acceleration, m s^{-2}
h_{sg}	interfacial heat transfer coefficient, $\text{W m}^{-2} \text{K}^{-1}$
h_v	volumetric heat transfer coefficient, $\text{W m}^{-3} \text{K}^{-1}$
H	height of the column, m
k	thermal conductivity, $\text{W m}^{-1} \text{K}^{-1}$
k_p	intrinsic permeability, m^2
l	Representative Elementary Volume length scale, m
L	system length scale, m
m	mass, kg
n	number of independent experiments
Nu	Nusselt number
P	pressure, Pa
Pr	Prandtl number
q	heat flux, W m^{-2}
Q	volumetric flow rate, $\text{m}^3 \text{s}^{-1}$
r	radius of the column, m
Ra	Rayleigh number
Re	Reynolds number
S	objective function, K^2
t	time, s
T	temperature, K
T_∞	ambient temperature, K
u_g	Darcy Air flux, m s^{-1}
U	global heat loss coefficient, $\text{W m}^{-2} \text{K}^{-1}$
V	volume, m^3

Greek symbols

α	thermal diffusivity, $\text{m}^2 \text{s}^{-1}$
δ_w	thickness of the thermal wave, m
μ	dynamic viscosity, Pa s
ν	kinematic viscosity, $\text{m}^2 \text{s}^{-1}$
ρ_b	bulk density, kg m^{-3}
ρ_s	particle density, kg m^{-3}
ϕ	porosity
σ	Stefan–Boltzmann constant, $\text{W m}^{-2} \text{K}^{-4}$
σ_s	standard deviation, K
τ_{REV}	Representative Elementary Volume characteristic time, s
τ_p	particle-scale characteristic time, s

Subscripts/superscript

avg	average
c	cylinder
cond	conduction
conv	convection
exp	experimental
f	final
g	gas
gen	generation
h	heater
i	time step
in	inlet
j	thermocouple number
M	mean
max	maximum
min	minimum
num	numerical
0	initial
out	outlet
p	peak
rad	radiation
s	solid (quartz)
sg	solid/gas
sp	sphere
st	standard
T	total
w	wall

$$\phi(\rho_g C_{p_g}) \frac{\partial T_g}{\partial t} + \rho_g C_{p_g} u_g \frac{\partial T_g}{\partial x} = \phi \frac{\partial}{\partial x} \left(k_g \frac{\partial T_g}{\partial x} \right) + h_{sg} \left(\frac{A_{s,sp}}{V_{sp}} \right) (T_s - T_g) \quad (2)$$

The two equations are linked by the interfacial heat transfer coefficient (h_{sg}), which dictates transfer between solid and gas phases. h_{sg} is multiplied by the surface area per unit volume assumed as perfect spheres ($A_{s,sp}/V_{sp} = 6(1 - \phi)/d_p$) [29]. The global heat loss coefficient (U) is multiplied by the surface area per unit volume of cylindrical column ($A_{s,c}/V_c = 2/r$). Note that source/sink terms would appear in Eqs. (1) and (2) if chemical reactions were taking place.

Analytical and numerical models of smouldering assuming LTE [7,18,20,29–37] and LTNE [21,22,38–45] have been extensively applied. It is suspected that LTNE is necessary to predict scenarios with forced air flow through hot sand. For example, high inlet gas velocities can decrease the solid temperature until smouldering quenches [1,38,46–52]. Thus, LTNE predictions require quantifying the thermophysical properties of both phases and h_{sg} .

The thermophysical properties of sand are important for a wide range of heat transfer applications beyond only applied smouldering. Sand's specific heat capacity (C_{ps}) and thermal conductivity (k_s) vary with temperature (T), porosity (ϕ), and particle diameter (d_p). Literature thermophysical properties for quartz sand are compiled in Table 1. The range of values reveal that these measurements need to be conducted with care and under relevant experimental conditions.

h_{sg} has been examined to predict heat transfer processes in a range of porous media including sand beds [62,63], sintered particles [64–66], spherical glass particles [67–69], ceramic foam [70–73], metal foam [74], and porous carbon foam [75]. h_{sg} is independent of the surface area per unit volume of the porous medium ($a_v = A_s/V$) (see Eq. (1)). When a_v is unknown, the results are reported in terms of a volumetric heat transfer coefficient ($h_v = a_v h_{sg}$) [70,71]. Analytical equations [23–26,42,66], inverse modelling [70,71], and experiments [66,70,71,76–83] have been used to derive empirical correlations for h_{sg} or h_v as a function of the parameters on which it depends, such as Reynolds number

Table 1
Literature values for thermophysical properties of sand.

Ref.	d_p [mm]	C_{ps} [J kg ⁻¹ K ⁻¹]	k_s [W m ⁻¹ K ⁻¹]	k_p [m ²]	ϕ [-]	ρ_b [kg m ⁻³]	T [°C]
[53]	0.76–0.91	776	4.2	–	–	2632	20–70
[54]	0.50–1.00	–	0.27–0.40	–	–	–	20–200
[55]	–	–	0.52	–	–	1730	–
[56]	0.38–1.70	840	–	–	0.31–0.38	1600–1800	–
[57]	–	–	0.23	1.8×10^{-9}	0.39–0.41	–	–
[58]	–	726	0.53–0.59	–	–	1630–1740	–
[59]	0.15–0.60	796	0.32–0.34	–	–	1400	–
[60]	–	–	0.3	–	–	–	–
[61]	–	800	0.27	–	–	1520	27
[62]	–	950	0.45	–	–	1700	–

($Re = \rho_g u_g d_p / \phi \mu_g$), Nusselt number ($Nu = h_{sg} d_p / k_g$), Prandtl number ($Pr = \mu_g C_{pg} / k_g$), ϕ , and d_p . Wakao et al. [78,84], conducting an extensive review of experiments in packed beds (Fig. 1), provided:

$$Nu = \frac{h_{sg} d_p}{k_g} = 2 + 1.1 (Re^{0.6} Pr^{1/3}) \quad (3)$$

which has become the correlation most widely employed.

A compilation of other empirical correlations is provided in Table 2. Many aspects of these correlations are inconsistent. For example, several studies found that h_{sg} increases [85,86] or decreases [65,66,69–71,87] with d_p , while others indicate the h_{sg} (d_p) relationship is affected by the solid and fluid thermal conductivities, Darcy air fluxes, and porosities [88,89]. In general, they agree that an increase in the Darcy air flux (u_g) (i.e., increase in Re) results in an increase in h_{sg} [65–67,69,74,87,90] up to a maximum beyond which it is independent of u_g [67,87,90].

Smouldering studies have extensively used Eq. (3) [78] to predict h_{sg} or h_v [22,38–40,44,93]. However, Leach et al. [22] concluded that Eq. (3) overestimates the heat transfer coefficient, resulting in an incorrect assumption of LTE for smouldering. A key issue is that Eq. (3) was developed for systems very different from smouldering. The packed bed systems considered for Eq. (3) exhibit $15 \leq Re \leq 8500$ and $30 \leq d_p \leq 171$ mm, which leads to Nu in the range 10^1 – 10^2 . In contrast, natural convection (i.e., accidental) smouldering typically exhibits $0.01 < Re < 0.1$ [50] and forced air (i.e., engineered) smouldering typically employs $1 < Re < 40$ [6, 8, 12, 14–16, 94–101] and $0.1 < d_p < 2$ mm [9, 12, 15, 16, 102], which corresponds to Nu in the range 10^{-4} – 10^1 . Therefore, smouldering

combustion is outside the range of applicability of Eq. (3), as illustrated in Fig. 1. No h_{sg} correlation exists for the specific conditions of applied smouldering, namely hot gases flowing through sand at relevant Re .

The main objective of this study is to develop an empirical correlation for h_{sg} between forced air and sand at the low Reynolds' numbers relevant to smouldering. Twelve column experiments were conducted to evaluate heat transfer in sand for different air fluxes and sand particle diameters. All of the necessary parameters were obtained independently except h_{sg} , which was optimized through inverse modelling of the experimental results. The developed correlation was validated against two additional experiments. A numerical model, equipped with the validated correlation, was then employed to explore the system's sensitivity to key parameters. In addition, the model allowed exploration of the validity of assuming local thermal equilibrium and this was compared to an analytical LTE criterion developed for these systems. The outcome is a new empirical Nu vs Re and Pr correlation that is valid for air flow through sand in conditions relevant to smouldering, namely $0.125 < d_p < 2.000$ mm, $Pr = 0.72$, and $0.5 < Re < 31$. This correlation is valuable for improving our understanding of thermal non-equilibrium in such systems and predicting h_{sg} in a variety of similar heat transfer scenarios.

2. Methodology

2.1. Experimental setup

Heat propagation and transfer experiments were carried out in a stainless-steel cylindrical column with 0.160 m inner diameter and 0.505 m in height (Fig. 2). The column was placed over a stainless-steel base (0.14 m inner diameter, 0.20 m in height), containing a flat, spiral-coiled heater (0.14 m outer diameter, 450 W, 120 V, Watlow Ltd) connected to a 120 V AC, single-phase variable power supply (STACO Energy Products), and an air diffuser made of perforated tubes connected to laboratory compressed air supply via a mass flow controller (FMA5400/5500 Series, 0–500 L min⁻¹, Omega Ltd). The air diffuser was covered with commercially available quartz sand (number 1240, Bell & MacKenzie Co., mean $d_p = 0.5$ mm, coefficient of uniformity < 1.5) to ensure uniform air-flow. The column was filled with clean quartz sand with one of three distinct particle diameters (Table 3). The particle diameters were obtained by sieving sands number 12ST, 1240, and 505 (Bell & MacKenzie Co.) and retaining only what remained on sieves number 16, 40, and 120, respectively, for the hereafter named “coarse”, “medium”, and “fine” sands. The sieved sands were carefully packed in 0.05 m lifts, each tamped, for maximum uniformity. Twelve thermocouples (3.2 mm diameter, 150 mm length, Type K, Inconel, Omega) were horizontally positioned at intervals of 0.035 m to measure the variation in temperature at the column centerline. The thermocouples were connected to a computer through a data logger (Multifunction Switch/Measure Unit

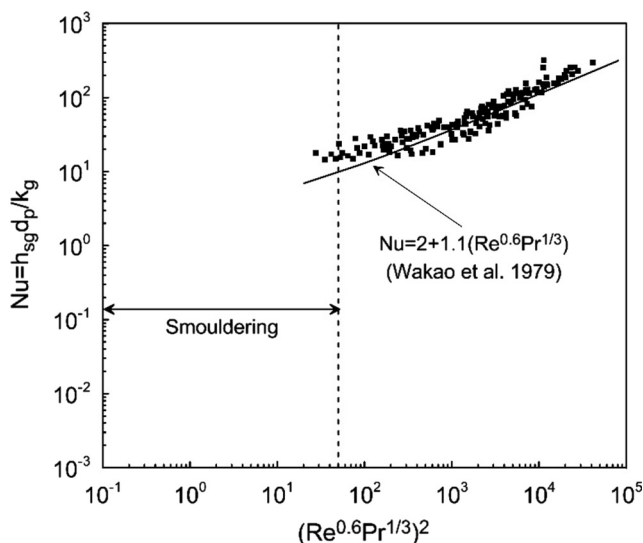


Fig. 1. Log-log plot of the experimental data (■) compiled by [78] along with Eq. (3) (solid black line). The data from [78] were reproduced with permission.

Table 2
Literature correlation equations for predicting the heat transfer coefficient in porous beds.

Ref.	Eq.	Correlation	Material	d_p (mm)	ϕ	Fluid	Re	Pr	Description
[41]	(4)	$Nu_p = \frac{h_p d_p}{k_p} = a + b Re^c$	Polyurethane foam	-	0.97–0.99	Air	-	-	Values of a , b , and c are empirical constants
[66]	(5)	$Nu = \frac{h_p d_p}{k_p} = 0.198 \phi^{0.07} Re^{0.66} Pr^{1/3}$	Sinter particles	12–32	0.49–0.54	Air	537–2233	0.67–0.70	-
[69]	(6)	$Nu = C Re^a Pr^b$	Spherical glass particles	11–22	-	Air	1000–5000	-	Values of a , b , and c are empirical constants
[70]	(7)	$Nu = 0.819 [1 - 7.33 (\frac{\phi}{4})] Re^{0.36 [1 + 15.5 (\frac{\phi}{4})]}$	Ceramic Foam	-	0.83–0.87	Air	5.1–564	-	The ratio d/L varies from 0.005 to 0.136, where d is the pore diameter and L is the thickness of the porous ceramic
[71]	(8)	$Nu_p = \frac{h_p d_p}{k_p} = C Re^m$	Cellular Ceramics	-	-	Air	0.02–1594	-	Values of C and m vary depending on the porous medium properties
[73]	(9)	$Nu_p = a Re^b$	Ceramic foams	-	-	Air	100–2000	-	Values of a and b are empirical constants
[74]	(10)	$Nu = b_1 Re^{b_2}$	Aluminum foams	-	0.70–0.95	Air	1900–7800	-	Values of b_1 and b_2 vary with porosity
[80]	(11)	$Nu = \left\{ (1.18 Re^{0.58})^4 + \left[\left(0.23 \left(\frac{Re}{1-\phi} \right)^{0.75} \right)^4 \right] \right\}^{1/4}$	Pebble beds	-	0.26–0.94	Air Helium	10–10 ⁵	0.71	-
[81]	(12)	$Nu_p = 0.124 (Re Pr)^{0.791}$	Open-cellular materials	-	0.74–0.95	Air	-	-	-
[82]	(13)	$Nu = 0.015 + 0.11 (Re)^{0.73}$	Shredded materials	-	0.80	Air	-	-	Valid for $Pe = Re Pr < 25$
[83]	(14)	$Nu_p = 0.07 \left(\frac{\phi}{1-\phi} \right)^{2/3} (Re Pr)$	Spherical particles	-	0.70–0.95	Air	3–1000	0.72	-
[91]	(15)	$Nu = 2.4 \times 10^{-5} + 285.6 (Re^{2.7} Pr^{1/3})$	Sand	0.3–1	0.30	Water	0.001–0.01	-	Based on h_{sg} calculated from [92]

34980A, Agilent) that acquired temperatures every 2 s. The column was wrapped in insulation (high-temperature mineral wool, McMaster-Carr) to minimize heat losses.

Table 3 summarizes the fourteen experiments that were performed. All experiments followed a heating procedure similar to that established for igniting a smouldering experiment [15,16]; however, no fuel was used in this study. Exps. 1–12 were used to develop the heat transfer correlation while Exps. A and B were used for model validation. In each experiment, the heat wave was initiated by providing power to the heater (90% capacity, 4.4A) for 1800 s. Then, air injection just below the heater was initiated and maintained at a constant Darcy air flux (volume per unit cross-sectional area per unit time). Darcy air fluxes ranged from 0.016 to 0.113 m s⁻¹, which correspond to volumetric flow rates from 20 to 140 L min⁻¹; this spans the range typically employed in applied smouldering studies [15,16,103]. After 600 s of air injection (i.e., 2400 s of heating) the heater was turned off while the air flow was maintained. Exp. B tripled the “pre-air” heating time to 5400 s, at which time the air flow was initiated and the heater was turned off at 6000 s. The base case experiment (1.18 < d_p < 2.00 mm, 0.065 m s⁻¹) was repeated five times to provide a measurement of the experimental uncertainty. Only three Darcy air fluxes (0.016, 0.040, and 0.065 m s⁻¹) were used for the fine sand because the sand fluidized at higher air fluxes.

2.2. Global energy balance

Heat losses play an important role in heat transfer systems. Although a rigorous analysis of heat loss effects requires multi-dimensional modelling [7,21,36], radial heat losses in these experiments may be quantified by the use of a global heat loss coefficient (U) and assuming a one-dimensional system. U was calculated through an energy balance:

$$E_{in} - E_{out} + E_{gen} - E_{loss} = \frac{dE_s}{dt} \quad (16)$$

The energy entering (E_{in}) the column comes from the heater (Fig. 2). Energy can leave the column vertically out the top (E_{out}) or through radial heat losses (E_{loss}). Since no chemical reactions occur, the energy generation term (E_{gen}) is zero, and the result is the rate at which energy stored in the system (E_s) changes. E_{in} and E_{out} are difficult to estimate since the gas enthalpy and heater energy are unknown. Therefore, the approach here was to isolate a time interval during which approximately zero energy is entering and leaving the system ($E_{in} = E_{out} = 0$); in other words, when both the inlet and outlet temperatures were approximately ambient (25–35 °C). This allows E_s in the time interval (i) to be calculated:

$$E_{s,i} = \sum_{j=1}^{12} [m_{s,j} C_{ps} (T_{s,j}(x) - T_{\infty})] \quad (17)$$

where the mass of sand in each control volume of the column ($m_{s,j}$) is calculated from the total mass of sand ($m_{s,T}$) divided by the number of thermocouples (j), which here is 12. The sand temperature in each control volume ($T_{s,j}$) was taken from the thermocouple at the axis of symmetry. The thermocouple was assumed to best represent the sand since the thermocouple's characteristic heating time is likely most consistent with the solid phase. If heat losses are occurring, Eq. (17) would show E_s decreasing with time during this interval (while adiabatic conditions would result in constant E_s). Since the control volume is small enough that the Biot number (Bi) is also small and radial heat losses (E_{loss}) are assumed, Eq. (16) becomes:

$$E_{loss} = -UA_{s,c} (T_{avg(t)} - T_{\infty}) = m_{s,T} C_{ps} \frac{dT_{avg(t)}}{dt} \quad (18)$$

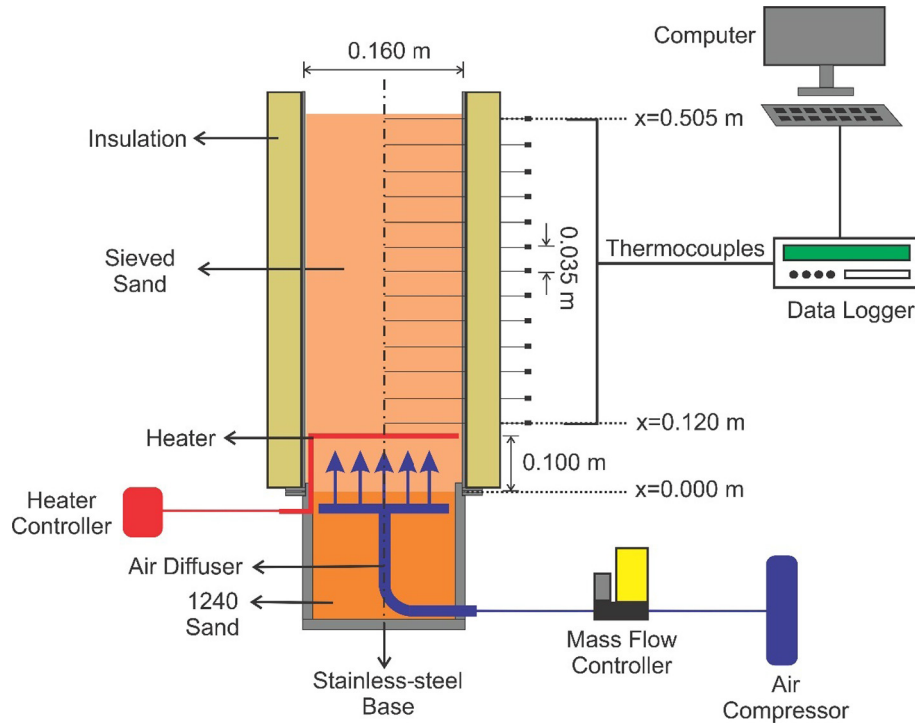


Fig. 2. Schematic of the experimental apparatus.

Table 3
Heat transfer experiments.

Exp. [#]	d_p [mm]	Q_g [L min ⁻¹]	u_g [m s ⁻¹]	Heating Period [s]	n [#]
1	1.180 < d_p < 2.000	20	0.016	2400	1
2		50	0.040	2400	1
3		80	0.065	2400	5
4		140	0.113	2400	1
5	0.425 < d_p < 0.600	20	0.016	2400	1
6		50	0.040	2400	1
7		80	0.065	2400	1
8		110	0.089	2400	1
9		140	0.113	2400	1
10	0.125 < d_p < 0.250	20	0.016	2400	1
11		50	0.040	2400	1
12		80	0.065	2400	1
A	1.180 < d_p < 2.000	110	0.089	2400	1
B		110	0.089	6000	1

which can be integrated over time to obtain U :

$$U = -\ln \left(\frac{T_{avg}(t_2) - T_\infty}{T_{avg}(t_1) - T_\infty} \right) \frac{m_{s,T} C_{ps}}{A_{s,c} (t_2 - t_1)} \quad (19)$$

The surface area of the cylinder is $A_{s,c} = 2\pi Hr$, C_{ps} was measured (see Section 2.3), T_∞ is the ambient temperature, t_2 and t_1 represent the time period over which Eq. (18) was integrated, and the mass-weighted average temperature was calculated:

$$T_{avg}(t) = \frac{\sum_{j=1}^{12} [m_{s,j} C_{ps} (T_{s,j}(x) - T_\infty)]}{m_{s,T} C_{ps}} \quad (20)$$

As the temperature of the system varies with time and distance, the purpose of Eq. (20) was to obtain an average temperature of the entire domain varying just with time. Overall, this approach uses the centerline thermocouple data from a particular interval in each experiment to estimate the fraction of energy decline at the centerline due to radial heat loss throughout the experiment.

2.3. Sand properties

The porosity (ϕ) and bulk density (ρ_b) of each sand pack was calculated using the mass of sand, the particle density (ρ_s) and the cell volume. The intrinsic permeability (k_p) of each sand was determined in a custom-built permeameter (following ASTM D6539-00 [104]). A Hot Disk Thermal Constants Analyzer [105] was used to measure k_s as a function of temperature for each sand. C_{ps} as a function of temperature was measured by Differential Scanning Calorimetry (DSC Q2000, TA Instruments) following ASTM-E1269 [106]. Further details are provided in Supplementary Information and supplied Refs. [104,105,107,108].

Table 4 presents the measured properties for all three sand sizes. As expected, ϕ and ρ_b varied little with d_p , and k_p increased two orders of magnitude from the smallest to the largest sand. As expected, k_s linearly increased with temperature for all three sands, as shown in Fig. 3. Note that the experimental uncertainty was $\pm 5\%$, and the maximum difference in k_s for all three sands

Table 4

Measurements of the sand properties.

d_p [mm]	T [°C]	k_s [W m ⁻¹ K ⁻¹]	ϕ [-]	ρ_b [kg m ⁻³]	k_p [m ²]
0.125 < d_p < 0.250	19.0	0.247	0.36	1691	2.07×10^{-11}
	86.0	0.278			
	175.0	0.325			
	269.0	0.359			
0.425 < d_p < 0.600	22.0	0.256	0.37	1660	1.84×10^{-10}
	85.0	0.308			
	172.0	0.348			
	264.0	0.391			
1.180 < d_p < 2.000	22.0	0.276	0.37	1672	1.03×10^{-9}
	85.0	0.322			
	173.0	0.382			
	267.0	0.432			

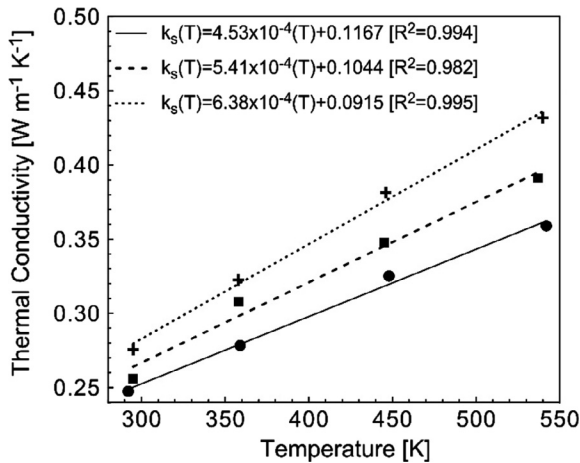


Fig. 3. Thermal conductivity of sand versus temperature increase for three particle diameters: +: 1.180 < d_p < 2.000 mm; ■: 0.425 < d_p < 0.600 mm; ●: 0.125 < d_p < 0.250 mm. Solid and dashed lines represent the linear regression for each particle diameter. The accuracy and reproducibility of each measurement were within $\pm 5\%$ and $\pm 2\%$, respectively [109].

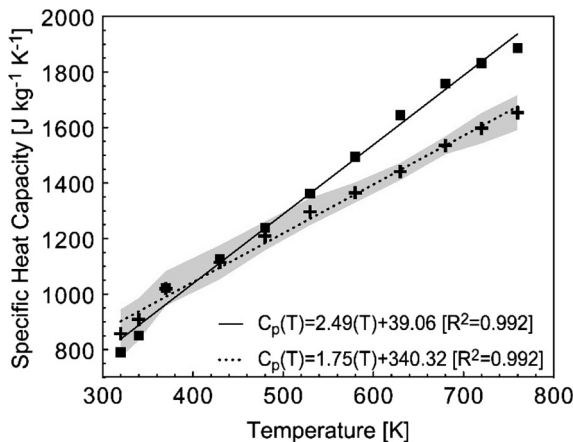


Fig. 4. C_p of sand versus temperature increase for two particle diameters (dashed line: linear regression for (+) 1.180 < d_p < 2.000 mm; solid line: linear regression for (■) 0.425 < d_p < 0.600 mm). Confidence intervals (shaded region) were evaluated based on three distinct experiments for 1.180 < d_p < 2.000 mm calculating the area under the standard normal curve that equals 95%.

was only 7%; it can therefore be concluded that k_s exhibits negligible dependence on d_p . Fig. 4 presents C_{ps} measurements for the medium (0.425 < d_p < 0.600 mm) and coarse (1.180 < d_p < 2.000 mm) sands. The DSC method did not provide reliable C_{ps} results

for the fine sand (0.125 < d_p < 0.250 mm). As expected, C_{ps} linearly increased with temperature, with a maximum value of 1886 J kg⁻¹ K⁻¹ (medium sand) and 1653 J kg⁻¹ K⁻¹ (coarse sand) at 760 K (486.85 °C). The experimental uncertainty for C_{ps} was found to be 5% and the maximum C_{ps} difference from coarse to medium sand was only 8%. Therefore, it is concluded that d_p has a negligible influence on C_{ps} . Moreover, the high C_{ps} values measured in this work confirm the widely held (but seldom tested) assumption that sand has a relatively high specific heat capacity.

3. Modelling

3.1. Governing equations

A one-dimensional numerical model was developed in COMSOL Multiphysics (Version 5.0), which uses the finite-element method. The domain simulated the 0.505 m column, with the lower boundary coincident with the air diffuser and the upper boundary at the sand's upper surface (Fig. 2). Air pressures and velocities were solved via the gas-phase continuity equation [110]:

$$\frac{\partial(\rho_g \phi)}{\partial t} + \frac{\partial(\rho_g u_g)}{\partial x} = 0 \quad (21)$$

which employed Darcy flow without gravity effects [111]. The gas density followed the ideal gas law [112]. The model solves the transient energy equation for both solid and gas phases, Eqs. (1) and (2), respectively; therefore, LTNE was considered. Heat transfer in the porous medium included conduction, convection, and radiation. Radiation heat transfer follows the Rosseland approximation [113] and was expressed as a radiative conductivity ($k_{rad} = 16\sigma d_p T_s^3/3$). An average global heat loss coefficient (U_{avg}) was included (see Sections 2.2 and 4.1), and used the surface area per unit volume ($A_{s,c}/V_c = 2/r$) of the column.

Sand particles were taken as spheres with a surface area per unit volume ($A_{s,sp}/V_{sp}$) equal to $6(1 - \phi)/d_p$ [29]. Sand properties, as described in Section 2.3, were employed and a homogeneous porous medium was assumed. As described above, direct measurements revealed no significant dependence on d_p for either k_s (Fig. 3) or C_{ps} (Fig. 4). Therefore, the determined k_s and C_{ps} for 0.425 < d_p < 0.600 mm were used in the simulations for all grain sizes. The properties of air - C_{pg} , k_g , and μ_g - were fitted from thermodynamic tables within 1% from 300 to 1500 K.

The initial and boundary conditions are provided in Table 5. Both heater and air diffuser were simulated by piecewise functions without smoothing effects. The air diffuser was described by a mass flux located at $x = 0$ m and the heater was described by a constant heat flux applied at $x = 0.100$ m. The piecewise functions followed the experimental procedure described in Section 2.1. The upper boundary was simulated by a convective heat flux at

Table 5
Initial and boundary conditions for numerical model.

Eq.	Initial condition	Boundary condition
(1), (2)	$t = 0 \Rightarrow \begin{cases} T_s = T_0 \\ T_g = T_0 \end{cases}$	$x = 0.100 \text{ m} \Rightarrow \begin{cases} -(k_s + k_{rad}) \frac{\partial T_s}{\partial x} = q \rightarrow 0 \leq t \leq t_h \\ -(k_s + k_{rad}) \frac{\partial T_g}{\partial x} = 0 \rightarrow t_h < t \leq t_f \\ T_g = T_0 \end{cases}$ $x = 0.505 \text{ m} \Rightarrow \begin{cases} -(k_s + k_{rad}) \frac{\partial T_s}{\partial x} = -U(T_s - T_\infty) \\ -k_g \frac{\partial T_g}{\partial x} = -U(T_g - T_\infty) \end{cases}$
(22)	$t = 0 \Rightarrow P_g = P_0$	$x = 0.000 \text{ m} \Rightarrow \rho_g u_g = \rho_g u_g(t) \rightarrow \begin{cases} u_g = 0 \rightarrow 0 \leq t \leq t_g \\ u_g = u_0 \rightarrow t_g < t \leq t_f \end{cases}$ $x = 0.505 \text{ m} \Rightarrow P_g = P_0$

Table 6
Model input parameters common to all simulations.

Parameters	Value	Unit	Reference
C_{ps}	$2.49(T_s) + 39.06$	$\text{J kg}^{-1} \text{K}^{-1}$	Measured
C_{pg}	$-3 \times 10^{-5}(T_g^2) + 0.2261(T_g) + 940.35$	$\text{J kg}^{-1} \text{K}^{-1}$	[114]
k_s	$0.000541(T_s) + 0.1044$	$\text{W m}^{-1} \text{K}^{-1}$	Measured
k_g	$-1 \times 10^{-8}(T_g^2) + 8 \times 10^{-5}(T_g) + 4.3 \times 10^{-3}$	$\text{W m}^{-1} \text{K}^{-1}$	[114]
$m_{s,T}$	14.1	kg	This work
μ_g	$-9 \times 10^{-12}(T_g^2) + 4 \times 10^{-8}(T_g) + 6 \times 10^{-6}$	Pa s	[114]
P_0	101,375	Pa	This work
q	25,000	W m^{-2}	Calculated
r	0.08	m	This work
ρ_s	2650	kg m^{-3}	[114]
T_0	293	K	This work
T_∞	293	K	This work
U	1.7	$\text{W m}^{-2} \text{K}^{-1}$	Calculated

$x = 0.505 \text{ m}$ and fixed atmospheric pressure. Table 6 presents the model input parameters for the base case, revealing that the majority were measured directly and the rest were obtained from the literature. The only exception was the interfacial heat transfer coefficient (h_{sg}), which needed to be determined independently (Section 3.2).

3.2. Inverse modelling

The only unknown parameter in the governing equations, h_{sg} , was obtained via inverse modelling of the experiments (Table 3). The objective function (S) minimized was:

$$S = \sum_{i=1}^{11} \sum_{j=1}^{t_f} (T_{s(\text{exp})}^{ij} - T_{s(\text{num})}^{ij})^2 \quad (22)$$

where $T_{s(\text{exp})}$ is the experimental (thermocouple) temperature assumed as a measurement of the solid (i.e. sand) phase (see Section 2.2) and $T_{s(\text{num})}$ is the simulated sand temperature at each thermocouple (i) and time step (j). The temperature curve for the first thermocouple above the heater ($x = 0.120 \text{ m}$) was not used in the h_{sg} optimization due to experimental variability in the heater position and the heat flux delivered at the inlet boundary. The rest of the thermocouples were used at all times. A unique h_{sg} was obtained for each experiment by varying h_{sg} only and minimizing S to best-fit the observed evolution of the heat wave. The Levenberg-Marquardt (LM) algorithm was used to minimize Eq. (22), which is a gradient-based optimization method available in the COMSOL Optimization Module. Further information on Levenberg-Marquardt algorithm can be found in [115–119].

3.3. LTE criterion

Kaviany [25] and Oliveira and Kaviany [27] present a framework for developing case-specific LTE criteria. They indicate that LTE can be assumed when the characteristic time (τ) associated with heat transfer at the scale of a representative elementary

volume (REV) is much greater than that at the scale of a single particle:

$$\tau_{REV} \gg \tau_p \quad (23)$$

In this work, this is evaluated by considering the energy balance between a sand particle and the air flowing past it. The developed LTE criterion for heat transfer associated with flowing air in hot sand is:

$$\frac{6h_{sg}}{u_g \rho_s C_{ps}} \gg 1 \quad (24)$$

The full derivation of Eq. (24) is presented in Supplementary Information. This LTE criterion was evaluated by employing (i) C_{ps} provided by the measurement (see Section 2.3) taken at the average temperature given in Eq. (20), and (ii) h_{sg} provided by the optimized value from the inverse modelling.

4. Results and discussion

Fig. 5a, showing temperature evolution in the base case experiment, demonstrates that conduction from the heater ($x = 0.100 \text{ m}$) extends only as far as the second thermocouple ($x = 0.155 \text{ m}$) just before the air was turned on ($t = 1800 \text{ s}$). The heating of the sand below the heater could not be shown due to the lack of thermocouples. Assuming symmetry of conduction suggests a heated zone 0.11 m thick centered on the heater. When air injection was initiated, convective heat transfer of this stored energy along the column was observed, starting with a rapid rise in the temperature of the first thermocouple above the heater ($x = 0.120 \text{ m}$). The heater was then turned off ($t = 2400 \text{ s}$) and the stored energy in the sand was transferred upwards and spread longitudinally, corresponding to a steady decrease in the peak temperature. This is clearly shown in Fig. 5b, which presents temperature profiles as a function of time. Fig. 5 also reveals the excellent repeatability of the experiment for temperatures in both space and time.

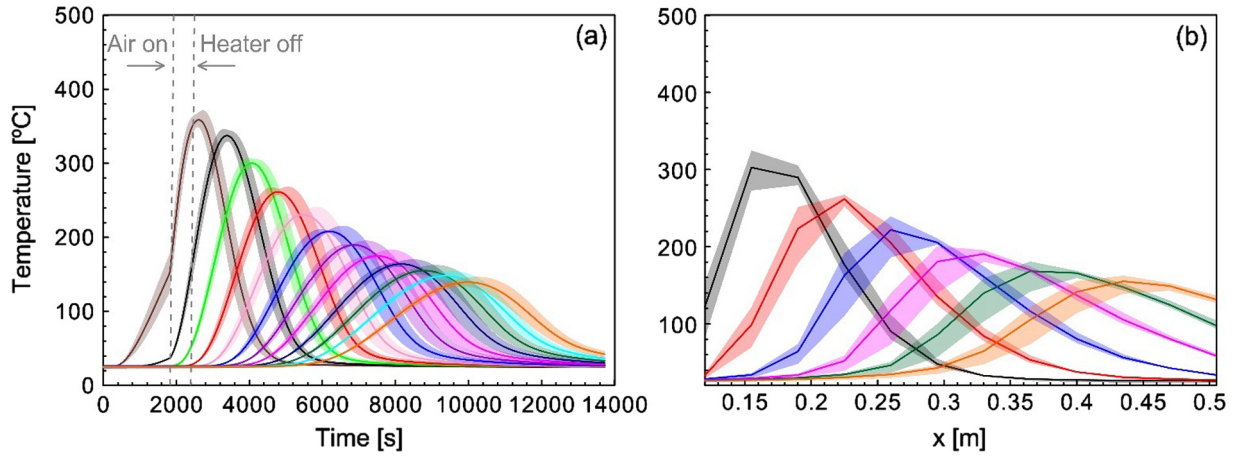


Fig. 5. (a) Experimental temperature evolution versus time and (b) temperature profile versus height of the column (x) for base case experiment ($1.18 < d_p < 2.00$ mm, 0.065 m s⁻¹). Solid lines represent the mean value of the temperatures (T_M) for five independent repeats (n). The colours in the figure (a) represent thermocouple positions (x) from 0.120 to 0.505 m with 0.035 m intervals, and (b) experimental times (t) from 3840 to 9240 s with intervals of 1080 s. The shading represents 95% confidence intervals. (For interpretation of the references to color in this figure legend, the reader is referred to the web version of this article.)

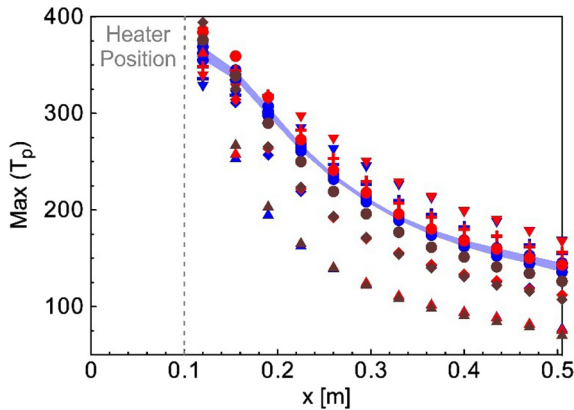


Fig. 6. Experimental peak temperature as a function of column height. The colours describe three sand particle diameters: blue ($1.180 < d_p < 2.000$ mm), red ($0.425 < d_p < 0.600$ mm), and brown ($0.125 < d_p < 0.250$ mm) and the symbols show five Darcy air fluxes: \blacktriangle (0.016 m s⁻¹), \blacklozenge (0.040 m s⁻¹), \bullet (0.065 m s⁻¹), $+$ (0.089 m s⁻¹), and \blacktriangledown (0.113 m s⁻¹). The shaded region corresponds to the 95% confidence interval for base case (0.065 m s⁻¹, $1.180 < d_p < 2.000$ mm). (For interpretation of the references to color in this figure legend, the reader is referred to the web version of this article.)

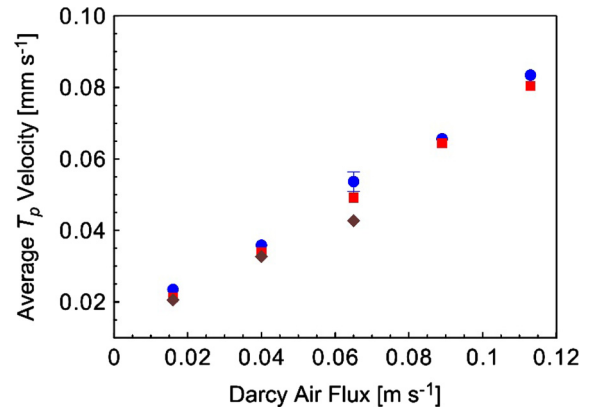


Fig. 7. Average peak temperature velocity as a function of Darcy air flux. The colours and symbols describe three sand particle diameters: \bullet ($1.180 < d_p < 2.000$ mm), \blacksquare ($0.425 < d_p < 0.600$ mm), and \blacklozenge ($0.125 < d_p < 0.250$ mm). The error bar shows the 95% confidence interval on the average velocity (0.065 m s⁻¹), \bullet ($1.180 < d_p < 2.000$ mm). (For interpretation of the references to color in this figure legend, the reader is referred to the web version of this article.)

The other experiments listed in Table 3 (except Exp. B) provide results that are similar to the base case, so the main trends are summarized in Figs. 6 and 7. Fig. 6 presents the peak temperature as a function of height for all experiments. First, it reveals a consistent decrease in the peak temperature as the heat wave proceeds through the column due to cooling processes. In addition, it shows that an increase in the Darcy air flux leads to an increase in the peak temperature. The velocity of the heat wave (Fig. 7) was calculated from the time interval necessary for two consecutive thermocouples reach their peak temperature and their known separation distance. Fig. 7 indicates that the speed of the heat wave is driven by convection. Taken together, the figures indicate that d_p has a negligible effect on both peak temperature and heat wave velocity (except for a minor effect for the cases of high Darcy air fluxes and fine sand).

Conduction versus convection dominance was analyzed via Eq. (S14) – Supplementary Information – and the results are presented in Fig. 8. The figure plots the ratio of the characteristic time for conduction to the characteristic time for convection for all of the experiments conducted and includes how the ratio changes as

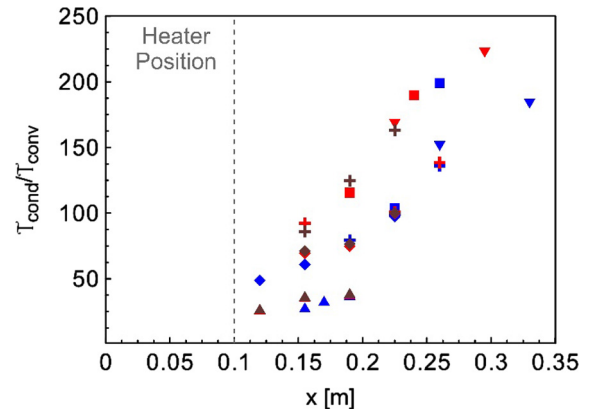


Fig. 8. The ratio between the characteristic time for conduction and the characteristic time for convection ($\tau_{\text{cond}}/\tau_{\text{conv}}$) as a function of heat wave position (x). The colours describe three sand particle diameters: blue ($1.180 < d_p < 2.000$ mm), red ($0.425 < d_p < 0.600$ mm), and brown ($0.125 < d_p < 0.250$ mm) and the symbols show five Darcy air fluxes: \blacktriangle (0.016 m s⁻¹), \blacklozenge (0.040 m s⁻¹), \bullet (0.065 m s⁻¹), $+$ (0.089 m s⁻¹), and \blacktriangledown (0.113 m s⁻¹). (For interpretation of the references to color in this figure legend, the reader is referred to the web version of this article.)

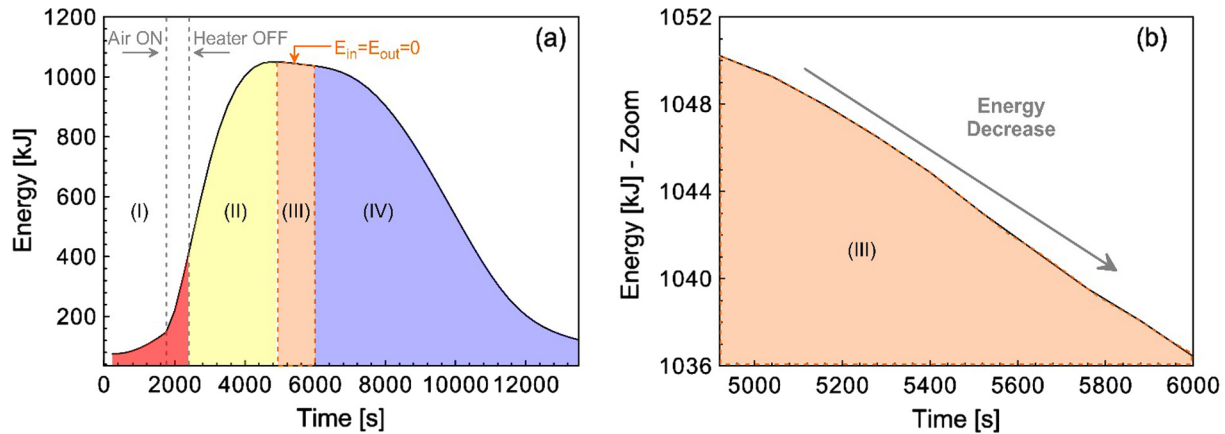


Fig. 9. (a) Energy evolution with time in the system and (b) zoomed into focus on Region (III) for the base case experiment ($1.18 < d_p < 2.00$ mm, and 0.065 m s⁻¹). Region (I) describes the period that the heater is powered; Region (II) shows the period of energy recovery after the heater has been shut off; Region (III) corresponds to the time-period between 4920 and 6000 s in which $E_{in} = E_{out} = 0$; Region (IV) defines the period in which energy is leaving the system via the outlet.

the heat wave propagates the length of the column. Convection is dominant when $\tau_{cond}/\tau_{conv} \gg 1$, thus Fig. 8 shows that heat transfer in all of the experiments are dominated by convection at all times. It also reveals that conduction is less important as the heat wave propagates away from the heater. Note that Fig. 8 shows negligible influence of d_p on this ratio. Supplementary Information also shows an analysis of mixed convection (buoyancy in forced convection) investigated via a Darcy-modified Rayleigh number (Ra) [120] (Eq. (S15)). The results indicate negligible Ra ($10^{-3} < Ra < 10^{-1}$); therefore, buoyancy in forced convection may be disregarded in this scenario.

4.1. Global heat loss coefficient (U)

Fig. 9a describes the energy in the system calculated from Eq. (18) for the base case experiment. The mass of sand and the adopted C_{ps} (measured in Section 2.3) are provided in Table 6. Note that C_{ps} for $0.425 < d_p < 0.600$ mm (retrieved at the average temperature) was used as the basis for the energy and all U values calculations. The figure identifies four distinct regions, of which Region (III) is of primary importance in this context because it represents the interval during which no energy was entering or leaving through the ends of the column (i.e., $E_{in} = E_{out} = 0$).

Under adiabatic conditions, Region (III) would be characterized by a constant amount of energy in the system. However, Fig. 9b reveals a decrease in stored energy with time, which means that heat losses are taking place. U was then calculated through Eq. (19) by applying $E_{in} = E_{out} = 0$ on Region (III). This was repeated for all experiments in which Region (III) could be isolated, namely all experiments but three (Table 7). Fig. 10 and Table 7, presenting the results of these calculations, illustrate that U varied from 1.0 to 2.0 W m⁻² K⁻¹ between experiments, which was smaller than the random error from five repeats. No clear relationship between U , d_p , and Re was observed. Therefore, the average U ($U_{avg} = 1.7$ W m⁻² K⁻¹) was employed as a constant heat loss coefficient in all model simulations. It should be noted that U_{avg} does not only represent heat losses across the column wall but also includes energy lost radially from the centerline of the column, a fraction of which is stored in sand between the centerline and the wall.

4.2. Interfacial heat transfer coefficient (h_{sg})

A value of h_{sg} was obtained for each experiment by inverse modelling (Section 3.2). For the base case, h_{sg} was 5.34 W m⁻² K⁻¹ and, in general, h_{sg} increased with increased Darcy air flux and with increased grain size up to a maximum of 10.43 W m⁻² K⁻¹

(Table 7). Fig. 12 shows that when the base case h_{sg} was input into the model, the simulated heat wave propagation was in excellent agreement with the experiment in both space and time.

This comparison between simulation and experiment was completed for all 12 cases. The fit was quantified in each case with the Normalized Root-Mean-Square Deviation (NRMSD) between experimental sand temperature ($T_{s,exp}$) and numerical sand temperature ($T_{s,num}$):

$$NRMSD = \frac{\sqrt{\sum_{i=1}^z (T_{s,exp} - T_{s,num})^2 / z}}{(T_{s,max} - T_{s,min})} \quad (25)$$

The NRMSD with respect to time evaluates inaccuracy associated with h_{sg} (e.g., Fig. 11a) while the NRMSD with respect to distance evaluated inaccuracy with respect to U (e.g., Fig. 11b). The NRMSD- h_{sg} and NRMSD- U values are listed for each experiment in Table 7. It reveals that, for the base case, the NRMSD values for both h_{sg} and U are 6%, which are within the 95% confidence interval for temperature versus time (9%) and temperature versus distance (9%) (see Fig. 5). Moreover, they reveal that the optimized h_{sg} values do reasonably well in providing simulations that match the observations. The lowest air flow rate shows up to 23% error, which might be related to uncertainty associated with assuming uniform values of sand thermal conductivity and specific heat capacity, since low air flow experiments experience a larger influence from conduction near the heater (see Fig. 8).

The NRMSD values in Table 7 reveal that the uncertainty associated with energy loss (U) is larger than associated with the heat transfer coefficient (h_{sg}) in all cases. A sensitivity analysis of the temperature curves to U (Fig. 12) for base case revealed that small variations in U ($0 < U < 3.6$ W m⁻² K⁻¹; i.e., the range associated with experimental repeatability) caused significant changes in the predicted peak temperatures. Assuming $U = 0$ W m⁻² K⁻¹ (adiabatic conditions) increased peak temperatures, as expected (see upper limit of grey shading on Fig. 12) resulting in an increase in the NRMSD- U from 6% to 12%. Assuming $U = 3.6$ W m⁻² K⁻¹ slightly overestimated the heat losses (see lower limit of orange shading on Fig. 12), increasing NRMSD- U from 6% to 7%. This illuminates the role of radial heat loss on the centerline temperatures and provides support for the independent method provided (Section 2.2) for determining its magnitude.

4.3. Evaluating the LTE criterion

Table 8 shows the results for the LTE evaluations against the criterion presented in Eq. (24), using the optimized h_{sg} values for each

Table 7

Summarized results for all experiments and simulations.

d_p [mm]	u_g [m s ⁻¹]	$E_{in} = E_{out} = 0$ [-]	U [W m ⁻² K ⁻¹]	h_{sg} [W m ⁻² K ⁻¹]	NRMSD- h_{sg} [%]	NRMSD- U [%]
1.180 < d_p < 2.000	0.016	✓	2.0	0.23	23	50
	0.040	✓	1.5	1.601	7	13
	0.065	✓	1.6 ± 1.1*	5.34 ± 0.2*	6 ± 0.1*	6 ± 0.1*
	0.113	×	–	10.43	6	10
0.425 < d_p < 0.600	0.016	✓	2.0	0.09	21	32
	0.040	✓	1.5	0.62	7	12
	0.065	✓	1.0	1.62	9	18
	0.089	×	–	3.00	17	32
	0.113	×	–	5.50	15	35
0.125 < d_p < 0.250	0.016	✓	2.0	0.04	17	35
	0.040	✓	1.9	0.30	19	29
	0.065	✓	1.8	0.35	10	16

* Based on 95% confidence interval.

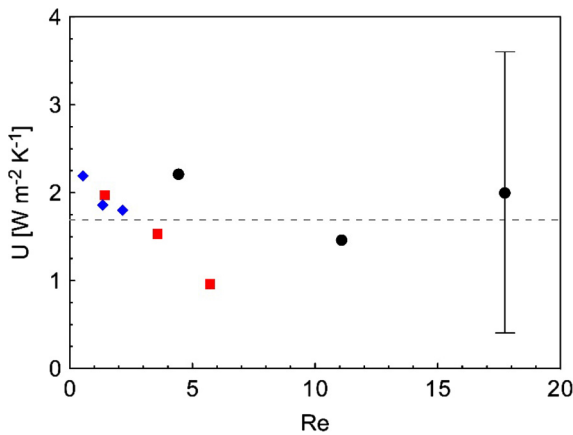


Fig. 10. Global heat loss coefficient calculated from Eq. (20) varying with Re number: (●) 1.180 < d_p < 2.000 mm; (■) 0.425 < d_p < 0.600 mm; (◆) 0.125 < d_p < 0.250 mm. The error bar encompasses the calculated range of values obtained for five repeat experiments at 0.065 m s⁻¹ and the dashed line corresponds to an average of all measured U values ($U_{avg} = 1.7$ W m⁻² K⁻¹).

experiment (Table 7). First, the table reveals that $Bi \ll 1$ for all experiments therefore, the bulk heating approximation assumed in Eq. (24) is valid. Moreover, it demonstrates that τ_{REV}/τ_p is much less than 1 for all cases. This means that LTNE is important in this scenario and the LTE assumption is invalid. Eq. (24) suggests that

h_{sg} in excess of 10⁵ W m⁻² K⁻¹ is required to assume LTE (compared to the maximum order of 10¹ W m⁻² K⁻¹ found in this work); however it is noted that the $Bi \ll 1$ assumption is violated when h_{sg} exceeds 180 W m⁻² K⁻¹.

4.4. New empirical correlation for the heat transfer coefficient

Fig. 13 plots the h_{sg} values from this work (Table 7) as a function of Nu , Re , and Pr . A power-law regression was employed that provides a new empirical correlation for the heat transfer between sand and air:

$$Nu = 0.001(Re^{1.97}Pr^{1/3}) \quad (26)$$

that is valid for $Pr = 0.72$, $0.5 < Re < 31$, and $0.125 < d_p < 2.000$ mm. The Prandtl number was added into Eq. (26) based on the boundary layer theory ($Pr^{1/3}$) [114].

Fig. 13 contrasts this new correlation, Eq. (26), with that most commonly used from the literature, Eq. (3). Note that the presented correlation captures low Re and Nu , which are outside the range of applicability of Eq. (3). Eq. (26) exhibits a higher slope than Eq. (3), which suggests an increased sensitivity of h_{sg} to Re in this region. Previous work has projected Eq. (3) to a $Re \sim 0$, predicting $Nu \sim 2$ for smouldering by natural convection [39]. This work reveals that such extrapolations of Eq. (3) would overestimate Nu by at least three orders of magnitude.

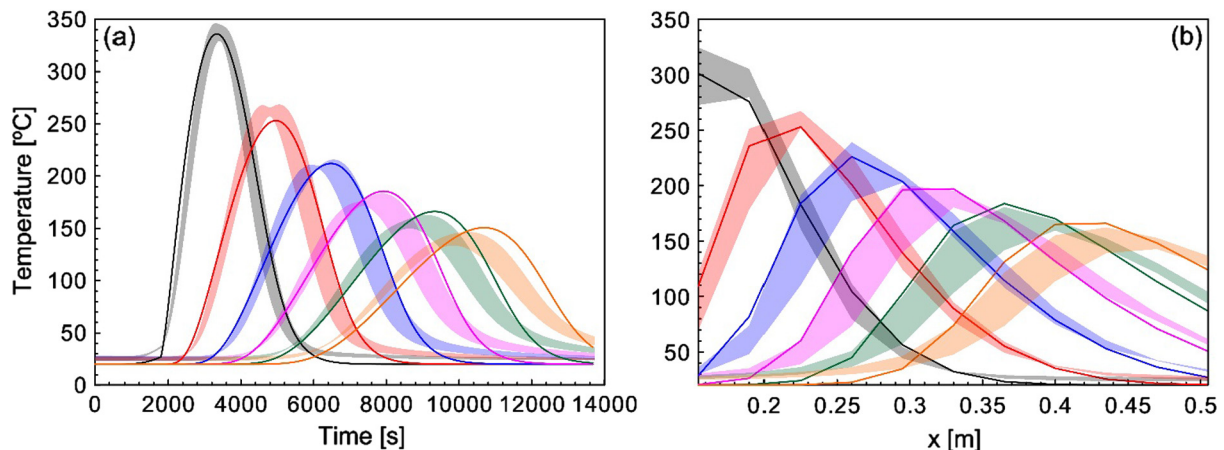


Fig. 11. (a) Temperature versus time and (b) temperature versus x showing a comparison between experimental (shaded region: 95% confidence interval) and numerical (solid line) data for base case (1.180 < d_p < 2.000 mm, 0.065 m s⁻¹). The colours show (a) thermocouple positions from 0.155 to 0.505 m with 0.07 m intervals, and (b) experimental times from 3840 to 9240 s with intervals of 1080 s. The numerical data shows the sand temperature for $U_{avg} = 1.7$ W m⁻² K⁻¹ and optimized $h_{sg} = 5.34$ W m⁻² K⁻¹. (For interpretation of the references to color in this figure legend, the reader is referred to the web version of this article.)

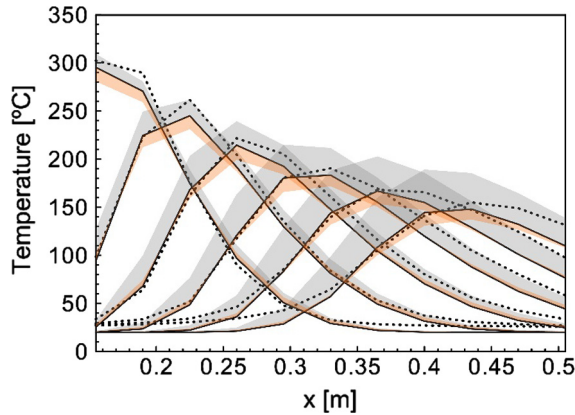


Fig. 12. Sensitivity of the temperature profiles to the heat loss coefficient (U). The dashed line shows the average experimental data for base case (0.065 m s^{-1} , $1.180 < d_p < 2.000 \text{ mm}$) and the solid line represents the simulated sand temperature employing $U = 1.7 \text{ W m}^{-2} \text{ K}^{-1}$ and optimized $h_{sg} = 5.34 \text{ W m}^{-2} \text{ K}^{-1}$ for times from 3840 to 9240 s with intervals of 1080 s. The upper limit of the grey region is the predicted temperature profiles for $U = 0 \text{ W m}^{-2} \text{ K}^{-1}$ (adiabatic) and the lower limit of the orange region represents $U = 3.6 \text{ W m}^{-2} \text{ K}^{-1}$. (For interpretation of the references to color in this figure legend, the reader is referred to the web version of this article.)

4.5. Validation

The developed correlation, Eq. (26), was input into the model as a function of h_{sg} and used to simulate two additional, distinct experiments (Exp. A and B, Table 3); these simulations employed no fitting or optimization. The predicted sand temperatures are compared to the experimental data in Fig. 14. The model predicted Exp. A (2400 s of heating) extremely well, with a NRMSD- $h_{sg} = 6\%$ (Fig. 14a) and NRMSD- $U = 7\%$ (Fig. 14b). The model prediction of Exp. B (6000 s of heating) was reasonable with a NRMSD- $h_{sg} = 13\%$ (Fig. 14c) and NRMSD- $U = 21\%$ (Fig. 14d). It is not surprising that this simulation was less accurate than for Exp. A since the heat losses in Exp. B would have been higher due to the higher peak temperatures (see Fig. 14). The U_{avg} value used for all simulations was developed from experiments with lower peak temperatures like Exp. A (see Section 4.1). The figure further shows that using the model equipped with the commonly used correlation, Eq. (3), is less able to reproduce validation Exp. A; in this case NRMSD- $h_{sg} = 14\%$ (Fig. 14e) and NRMSD- $U = 22\%$ (Fig. 14f).

4.6. Temperature difference between sand and air

The simulation of each experiment provides the temperatures of both phases, which are unattainable from the experiments

themselves. Fig. 15 plots the difference between the sand and gas temperatures along the length of the column normalized to the maximum (experimental) peak temperature ($\Delta T_{sg}/T_p$). LTE is approached as this ratio approaches zero. The figure illustrates that the Exp. A validation simulation shows $\Delta T_{sg}/T_p = 12\%$ near the heater and decreasing with distance to less than 5% due to reduced heater influence and increased convective cooling of the sand. The figure shows that the extended heating of Exp. B results in $\Delta T_{sg}/T_p = 23\%$ near the heater, decreasing along the column to less than 6%. Note that the model generally predicts the gas phase temperature is higher at the peak of the heat wave, but at certain distance and times the sand temperature is higher. When these experiments are simulated using Eq. (3) to dictate h_{sg} , $\Delta T_{sg}/T_p$ never exceeds 2%; nearly identical results are found when using an arbitrarily high, constant value of $h_{sg} = 500 \text{ W m}^{-2} \text{ K}^{-1}$ (Fig. 15). The average $\Delta T_{sg}/T_p$ for Exp. A is 6% and for Exp. B is 9%, while for the latter two simulations in Fig. 15 are 1% and 0.3%. The average $\Delta T_{sg}/T_p$ for all of the simulated experiments are shown in Table 8; these metrics provide additional evidence that LTE is not achieved in this system.

5. Conclusions and summary

Many systems of interest involve a heat wave travelling via flowing air through a fixed bed of fine to coarse sand at low

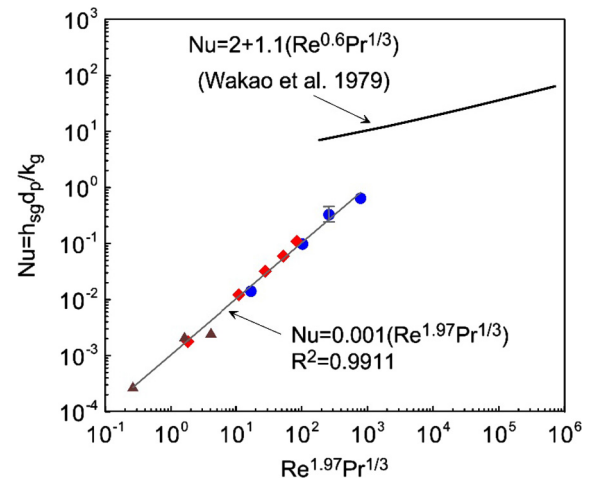


Fig. 13. Log-log plot describing h_{sg} as a function of Nu versus Re and Pr for three sand particle diameters (\bullet : $1.180 < d_p < 2.000 \text{ mm}$; \blacklozenge : $0.425 < d_p < 0.600 \text{ mm}$; \blacktriangle : $0.125 < d_p < 0.250 \text{ mm}$). The solid grey line shows the power law regression corresponding to Eq. (26). The solid black line shows the most commonly used correlation from the literature, Eq. (3).

Table 8
Evaluation of LTE criterion.

d_p [mm]	u_g [m s^{-1}]	τ_p [s]	τ_{REV} [s]	τ_{REV}/τ_p [-]	Bi [-]	$\Delta T_{sg}/T_p$ [%]
$1.180 < d_p < 2.000$	0.016	2.6×10^3	3.7×10^{-2}	1.4×10^{-5}	1.3×10^{-3}	22
	0.040	3.9×10^2	1.5×10^{-2}	3.8×10^{-5}	8.9×10^{-3}	10
	0.065	7.4×10^1	9.0×10^{-3}	1.2×10^{-4}	4.7×10^{-2}	6
	0.113	5.9×10^1	5.2×10^{-3}	8.8×10^{-5}	5.6×10^{-2}	6
$0.425 < d_p < 0.600$	0.016	2.2×10^3	1.2×10^{-2}	5.4×10^{-6}	1.6×10^{-4}	20
	0.040	3.2×10^2	4.7×10^{-3}	1.5×10^{-5}	1.1×10^{-3}	9
	0.065	1.2×10^2	3.0×10^{-3}	2.4×10^{-5}	2.9×10^{-3}	7
	0.089	6.6×10^1	2.0×10^{-3}	3.2×10^{-5}	5.4×10^{-3}	7
	0.113	3.5×10^1	1.7×10^{-3}	4.8×10^{-5}	1.0×10^{-2}	6
$0.125 < d_p < 0.250$	0.016	1.8×10^3	4.2×10^{-3}	2.3×10^{-6}	2.6×10^{-5}	19
	0.040	2.4×10^2	1.7×10^{-3}	7.0×10^{-6}	2.0×10^{-4}	9
	0.065	2.0×10^2	1.0×10^{-3}	5.1×10^{-6}	2.3×10^{-4}	7

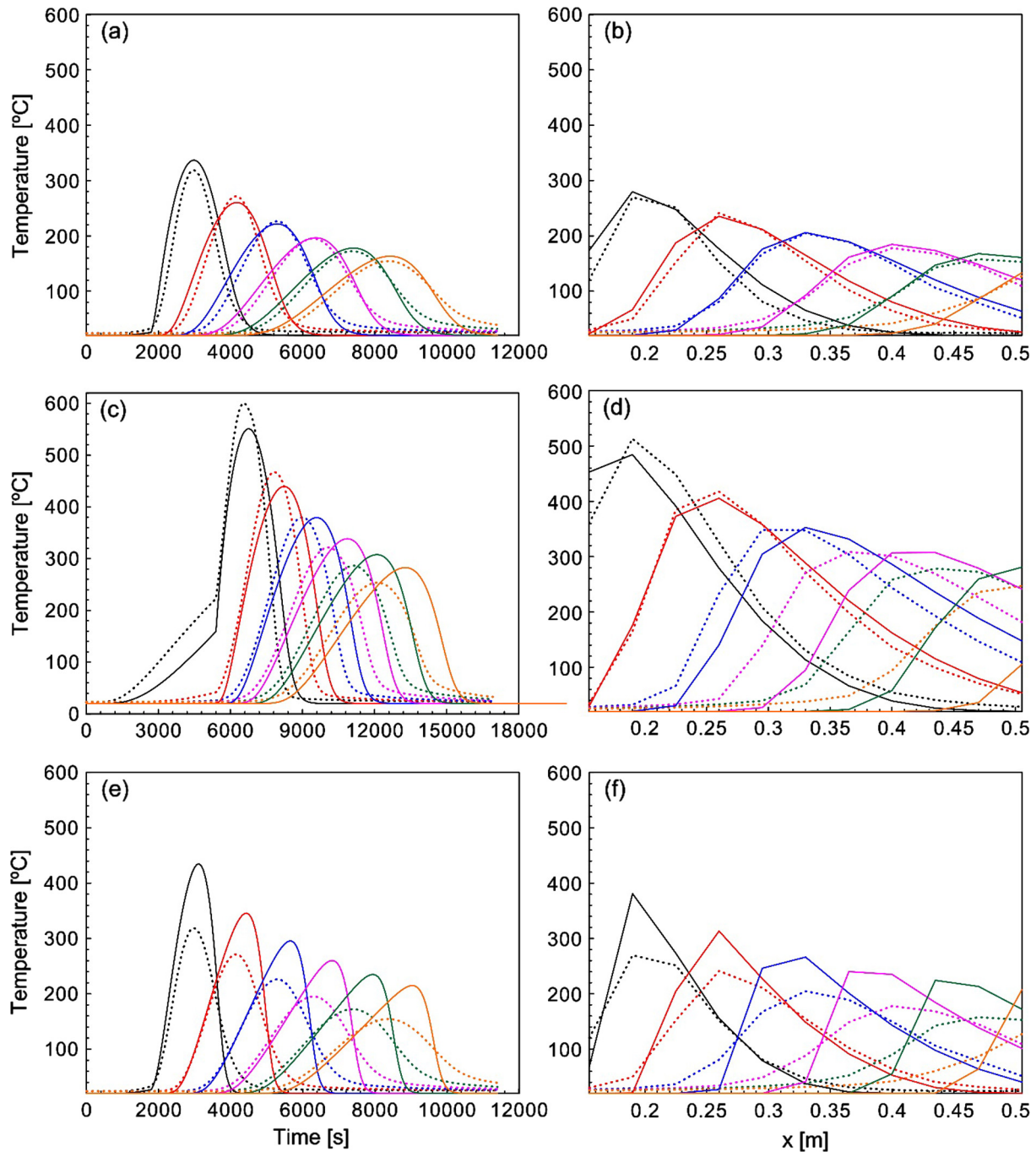


Fig. 14. Comparison of simulations (solid lines) to experiments (dashed lines). (a,b) Simulation using Eq. (26) for validation Exp. A (2400 s of heating) and (c,d) for validation Exp. B (6000 s of heating). (e,f) Simulation using Eq. (3) for validation Exp. A. The left column shows temperature-time with colours indicating thermocouple positions from 0.155 to 0.505 m at 0.07 m intervals. The right column shows temperature-height with experimental times from (b,f) 3840 to 9240 s with 1080 s intervals or (d) experimental times from 7500 to 15,000 s with intervals of 1500 s. (For interpretation of the references to color in this figure legend, the reader is referred to the web version of this article.)

Reynold's numbers ($Re < 30$). Such systems are typically assumed to be at local thermal equilibrium. When local thermal non-equilibrium is assumed, the heat transfer coefficient (h_{sg}) is typically calculated using the correlation of Wakao et al. [78,84]. This work identified that Wakao et al. [78,84] correlation was developed from high Reynold's numbers experiments ($15 \leq Re \leq 8500$) and can over-predict Nu by up to three orders of magnitude when extrapolated to low Re . It also demonstrated that the h_{sg} values produced by that correlation for these systems ($180 < h_{sg} < 420 \text{ W m}^{-2} \text{ K}^{-1}$) effectively generate local thermal equilibrium, which is not appropriate for these systems.

Twelve column experiments were conducted with a variety of sand sizes and air flow rates, providing a novel data set for heat wave propagation relevant to these systems. These were simulated with a one-dimensional numerical model that assumed local thermal non-equilibrium. All of the material properties and system parameters were obtained independently except h_{sg} , which was optimized via inverse modelling. A methodology for estimating heat losses based on a global energy balance in the experimental system demonstrated that radial heat losses were significant and needed to be included. The determined values of h_{sg} , which varied from 0.04 to $10.43 \text{ W m}^{-2} \text{ K}^{-1}$, were used to develop a new

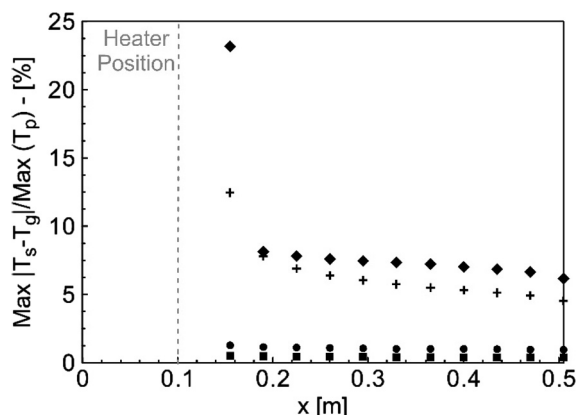


Fig. 15. Normalized maximum simulated solid (T_s) and gas (T_g) temperature varying with column height (x) for: (+) validation of Exp. A; (♦) validation of Exp. B; (●) Exp. A using Eq. (3); (■) Exp. A using $h_{sg} = 500 \text{ W m}^{-2} \text{ K}^{-1}$.

correlation: $Nu = 0.001(Re^{1.97}Pr^{1/3})$, which is valid for $0.5 < Re < 31$ and $0.125 < d_p < 2.000 \text{ mm}$. The numerical model employing this correlation was validated against two distinct experiments, producing excellent predictions of the measured temperatures even for significantly higher peak temperatures than considered in the development (e.g., characteristic of smouldering).

A new criterion for assuming local thermal equilibrium was developed based on characteristic time scales. Its application to these experiments demonstrated that the local thermal equilibrium assumption is incorrect for these low Reynold's number systems. Indeed, the validated model predicts temperatures differences between the air and sand of up to 23% in certain locations and up to 6% on average. When the model employed the Wakao et al. [78,84] correlation, negligible non-equilibrium was predicted locally and the model could not accurately reproduce the experiments. The high heat capacity of the sand combined with the dominance of convection in these systems acts to ensure that non-equilibrium must be considered in all of these cases, with increasing error in assuming equilibrium at lower air flow rates, smaller grain sizes, and increased proximity to the heater.

Overall, the new correlation was demonstrated to be reliable for simulating heat transfer between flowing air and a fixed sand bed. The fact that the model was able to predict low and high temperature processes with such low deviation indicates its robustness and wide applicability. This work is expected to be useful for understanding local thermal non-equilibrium in a variety of processes characterized by low Reynolds' numbers. Future work is exploring the value of this correlation in predicting the performance of ambient and applied smouldering systems.

Conflict of interest

None declared.

Acknowledgements

This research was supported by grants to the corresponding author including an Ontario Research Fund grant from the Ontario Ministry of Research, Innovation, and Science as well as a CREATE grant from the National Sciences and Engineering Research Council of Canada. We acknowledge the assistance of the Fire Safety Engineering team and the UQ Composites Group at the University of Queensland with the sand thermal properties measurements. Special thanks to Jeronimo Carrascal, Dr. Cristián Maluk, and Dr. Michael Heitzmann. We acknowledge the valuable comments of an anonymous review that helped improve the manuscript.

Appendix A. Supplementary material

Supplementary data associated with this article can be found, in the online version, at <http://dx.doi.org/10.1016/j.ijheatmasstransfer.2017.06.020>.

References

- [1] T.J. Ohlemiller, Modeling of smoldering combustion propagation, *Prog. Energy Combust. Sci.* 11 (4) (1985) 277–310.
- [2] K.N. Palmer, Smouldering combustion in dusts and fibrous materials, *Combust. Flame* 1 (2) (1957) 129–154.
- [3] J.L. Torero, A.C. Fernandez-Pello, Forward smolder of polyurethane foam in a forced air flow, *Combust. Flame* 106 (1–2) (1996) 89–109.
- [4] G. Rein, Smouldering combustion phenomena in science and technology, *Int. Rev. Chem. Eng.* 1 (2009) 3–18.
- [5] A. Bar-Ilan, G. Rein, D.C. Walther, A.C. Fernandez-Pello, J.L. Torero, D.L. Urban, The effect of buoyancy on opposed smoldering, *Combust. Sci. Technol.* 176 (12) (2004) 2027–2055.
- [6] M.F. Martins, S. Salvador, J.F. Thovet, G. Debenest, Co-current combustion of oil shale - Part 2: Structure of the combustion front, *Fuel* 89 (1) (2010) 133–143.
- [7] H. Fadaei, M. Sennoune, S. Salvador, A. Lapene, G. Debenest, Modelling of non-consolidated oil shale semi-coke forward combustion: influence of carbon and calcium carbonate contents, *Fuel* 95 (2012) 197–205.
- [8] G. Debenest, V. Mourzenko, J. Thovet, Smouldering in fixed beds of oil shale grains. A three-dimensional microscale numerical model, *Combust. Theory Modell.* 9 (1) (2005) 113–135.
- [9] L. Yermán, R.M. Hadden, J. Carrascal, I. Fabris, D. Cormier, J.L. Torero, J.L. Gerhard, M. Krajcovic, P. Pironi, Y.-L. Cheng, Smouldering combustion as a treatment technology for faeces: exploring the parameter space, *Fuel* 147 (2015) 108–116.
- [10] A.W. Bhutto, A.A. Bazmi, G. Zahedi, Underground coal gasification: from fundamentals to applications, *Prog. Energy Combust. Sci.* 39 (1) (2013) 189–214.
- [11] J.-P. Vantelon, B. Lodeho, S. Pignoux, J.L. Ellzey, J.L. Torero, Experimental observations on the thermal degradation of a porous bed of tires, *Proc. Combust. Inst.* 30 (2) (2005) 2239–2246.
- [12] T.L. Rashwan, J.L. Gerhard, G.P. Grant, Application of self-sustaining smouldering combustion for the destruction of wastewater biosolids, *Waste Manage.* 50 (2016) 201–212.
- [13] P. Pironi, Smouldering Combustion of Liquids in Porous Media for Remediating NAPL-Contaminated Soils PhD Thesis, University of Edinburgh, Edinburgh, Scotland, UK, 2009.
- [14] P. Pironi, C. Switzer, J.L. Gerhard, G. Rein, J.L. Torero, Self-sustaining smouldering combustion for NAPL remediation: laboratory evaluation of process sensitivity to key parameters, *Environ. Sci. Technol.* 45 (7) (2011) 2980–2986.
- [15] P. Pironi, C. Switzer, G. Rein, A. Fuentes, J.L. Gerhard, J.L. Torero, Small-scale forward smouldering experiments for remediation of coal tar in inert media, *Proc. Combust. Inst.* 32 (2) (2009) 1957–1964.
- [16] C. Switzer, P. Pironi, J.L. Gerhard, G. Rein, J.L. Torero, Self-sustaining smouldering combustion: a novel remediation process for non-aqueous-phase liquids in porous media, *Environ. Sci. Technol.* 43 (15) (2009) 5871–5877.
- [17] T.J. Ohlemiller, Smoldering combustion, in: P.J. DiNenno, D. Drysdale, C. L. Beyler, W.D. Walton (Eds.), *SFPE Handbook of Fire Protection Engineering*, National Fire Protection Association, Quincy, MA, USA, 2002, pp. 200–210.
- [18] A.P. Aldushin, I.E. Rumanov, B.J. Matkowsky, Maximal energy accumulation in a superadiabatic filtration combustion wave, *Combust. Flame* 118 (1–2) (1999) 76–90.
- [19] M.R. Henneke, J.L. Ellzey, Modeling of filtration combustion in a packed bed, *Combust. Flame* 117 (4) (1999) 832–840.
- [20] D.A. Schult, B.J. Matkowsky, V.A. Volpert, A.C. Fernandez-Pello, Forced forward smolder combustion, *Combust. Flame* 104 (1–2) (1996) 1–26.
- [21] G. Rein, A. Carlos Fernandez-Pello, D.L. Urban, Computational model of forward and opposed smoldering combustion in microgravity, *Proc. Combust. Inst.* 31 (2) (2007) 2677–2684.
- [22] S.V. Leach, G. Rein, J.L. Ellzey, O.A. Ezekoye, J.L. Torero, Kinetic and fuel property effects on forward smoldering, *Combust. Flame* 120 (3) (2000) 358.
- [23] M. Quintard, S. Whitaker, One- and two-equation models for transient diffusion processes in two-phase systems, *Adv. Heat Transfer* (1993) 369–464.
- [24] M. Quintard, S. Whitaker, Local thermal equilibrium for transient heat conduction: theory and comparison with numerical experiments, *Int. J. Heat Mass Transfer* 38 (15) (1995) 2779–2796.
- [25] M. Kaviany, *Principles of Heat Transfer in Porous Media*, Springer, 1995.
- [26] S. Whitaker, Improved constraints for the principle of local thermal equilibrium, *Ind. Eng. Chem. Res.* 30 (5) (1991) 983–997.
- [27] A.A.M. Oliveira, M. Kaviany, Nonequilibrium in the transport of heat and reactants in combustion in porous media, *Prog. Energy Combust. Sci.* 27 (5) (2001) 523–545.

- [28] D.A.A. Nield, A.A. Bejan, *Heat Transfer Through a Porous Medium*, second ed., Springer Verlag, 1999.
- [29] M. Fatehi, M. Kaviany, Adiabatic reverse combustion in a packed bed, *Combust. Flame* 99 (1) (1994) 1–17.
- [30] H. Chen, G. Rein, N. Liu, Numerical investigation of downward smoldering combustion in an organic soil column, *Int. J. Heat Mass Transf.* 84 (2015) 253–261.
- [31] F. He, N. Zobel, W. Zha, F. Behrendt, Effects of physical properties on one-dimensional downward smoldering of char: numerical analysis, *Biomass Bioenerg.* 33 (8) (2009) 1019–1029.
- [32] D.A. Schult, B.J. Matkowsky, V.A. Volpert, A.C. Fernandez-Pello, Propagation and extinction of forced opposed flow smolder waves, *Combust. Flame* 101 (4) (1995) 471–490.
- [33] C. Di Blasi, Mechanisms of two-dimensional smoldering propagation through packed fuel beds, *Combust. Sci. Technol.* 106 (1–3) (1995) 103–124.
- [34] S.S. Dosanjh, P.J. Pagni, A.C. Fernandez-Pello, Forced cocurrent smoldering combustion, *Combust. Flame* 68 (2) (1987) 131–142.
- [35] M.S.K. Youtsos, E. Mastorakos, Numerical simulation of thermal and reaction waves for in situ combustion in hydrocarbon reservoirs, *Fuel* 108 (2013) 780–792.
- [36] I.Y. Akkurtlu, Y.C. Yortsos, The dynamics of in-situ combustion fronts in porous media, *Combust. Flame* 134 (3) (2003) 229–247.
- [37] X. Huang, G. Rein, H. Chen, Computational smoldering combustion: predicting the roles of moisture and inert contents in peat wildfires, *Proc. Combust. Inst.* 35 (3) (2015) 2673–2681.
- [38] S.V. Leach, J.L. Ellzey, O.A. Ezekoye, A numerical study of reverse smoldering, *Combust. Sci. Technol.* 130 (1–6) (1997) 247–267.
- [39] A. Rostami, J. Murthy, M. Hajaligol, Modeling of a smoldering cigarette, *J. Anal. Appl. Pyrol.* 66 (1–2) (2003) 281–301.
- [40] B.-S. Jia, M.-Z. Xie, H. Liu, Numerical study on the propagation characteristics of forward smoldering in a cellulosic packed bed, *J. Shanghai Univ. (English Edition)* 12 (2) (2008) 171–179.
- [41] A.B. Dodd, C. Lautenberger, C. Fernandez-Pello, Computational modeling of smolder combustion and spontaneous transition to flaming, *Combust. Flame* 159 (1) (2012) 448–461.
- [42] C. Yang, J.F. Thovort, G. Debenest, Upscaling of mass and thermal transports in porous media with heterogeneous combustion reactions, *Int. J. Heat Mass Transf.* 84 (2015) 862–875.
- [43] C. Yang, G. Debenest, Numerical simulations for smoldering in a horizontal channel: comparisons between variable density-based formulation and incompressible one, *Combust. Sci. Technol.* 186 (12) (2014) 1954–1974.
- [44] N.C. Roy, Y. Nakamura, Investigation of unsteady behaviors of forward and opposed flow combustion of solid fuel, *Combust. Flame* 163 (2016) 517–531.
- [45] G. Debenest, V.V. Mourzenko, J.F. Thovort, Smoldering in fixed beds of oil shale grains: governing parameters and global regimes, *Combust. Theor. Model.* 9 (2) (2005) 301–321.
- [46] S.D. Tse, A.C. Fernandez-Pello, K. Miyasaka, Controlling mechanisms in the transition from smoldering to flaming of flexible polyurethane foam, *Symp. (Int.) Combust.* 26 (1) (1996) 1505–1513.
- [47] R. Hadden, A. Alkatib, G. Rein, J.L. Torero, Radiant ignition of polyurethane foam: the effect of sample size, *Fire Technol.* 50 (3) (2014) 673–691.
- [48] J.L. Torero, A.C. Fernandez-Pello, D. Urban, Experimental observations of the effect of gravity changes on smoldering combustion, *AIAA J.* 32 (5) (1994) 991–996.
- [49] M.K. Anderson, R.T. Sleight, J.L. Torero, Downward smolder of polyurethane foam: ignition signatures, *Fire Saf. J.* 35 (2) (2000) 131–147.
- [50] J.L. Torero, A.C. Fernandez-Pello, Natural convection smolder of polyurethane foam, upward propagation, *Fire Saf. J.* 24 (1) (1995) 35–52.
- [51] A.P. Aldushin, A. Bayliss, B.J. Matkowsky, Is there a transition to flaming in reverse smolder waves?, *Combust. Flame* 156 (12) (2009) 2231–2251.
- [52] J.L. Torero, A.C. Fernandez-Pello, M. Kitano, Opposed forced flow smoldering of polyurethane foam, *Combust. Sci. Technol.* 91 (1–3) (1993) 95–117.
- [53] M.A. Izquierdo-Barrientos, C. Sobrino, J.A. Almendros-Ibáñez, Experimental heat transfer coefficients between a surface and fixed and fluidized beds with PCM, *Appl. Therm. Eng.* 78 (2015) 373–379.
- [54] M.F. Martins, *The Structure of a Combustion front Propagating in a Fixed Bed of Crushed Oil Shale: Co-Current Configuration*, PhD Thesis, Université de Toulouse, 2008.
- [55] K. Manohar, D.W. Yarbrough, J.R. Booth, Measurement of apparent thermal conductivity by the thermal probe method, *J. Test. Eval.* 28 (5) (2000) 345–351.
- [56] S. Peng, N. Wang, J. Chen, Steam and air co-injection in removing residual TCE in unsaturated layered sandy porous media, *J. Contam. Hydrol.* 153 (2013) 24–36.
- [57] J. Gudbjerg, T.O. Sonnenborg, K.H. Jensen, Remediation of NAPL below the water table by steam-induced heat conduction, *J. Contam. Hydrol.* 72 (1–4) (2004) 207–225.
- [58] S.M. Farouq, Ali, Steam Injection, Secondary and Tertiary Oil Recovery Process, Interstate Oil Compact Commission, Oklahoma, City, 1974.
- [59] K. Manohar, R. Shirish, Apparent thermal conductivity of sand, *Int. J. Heat Exch.* 6 (1) (2005) 125–134.
- [60] G. Papadakis, P. Giaglaras, S. Kyritsis, A numerical method for determining thermal conductivity of porous media from in-situ measurements using a cylindrical heat source, *J. Agric. Eng. Res.* 45 (1990) 281–293.
- [61] M.J. Moran, H.N. Shapiro, D.D. Boettner, M.B. Bailey, *Fundamentals of Engineering Thermodynamics*, Wiley, 2010.
- [62] L. Chen, Y. Wang, L. Peng, P. Fu, H. Jiang, Study on the interfacial heat transfer coefficient between AZ91D magnesium alloy and silica sand, *Exp. Therm. Fluid Sci.* 54 (2014) 196–203.
- [63] G. Palumbo, V. Piglionico, A. Piccininni, P. Guglielmi, D. Sorgente, L. Tricarico, Determination of interfacial heat transfer coefficients in a sand mould casting process using an optimised inverse analysis, *Appl. Therm. Eng.* 78 (2015) 682–694.
- [64] P.X. Jiang, R.N. Xu, W. Gong, Particle-to-fluid heat transfer coefficients in miniporous media, *Chem. Eng. Sci.* 61 (22) (2006) 7213–7222.
- [65] P.-X. Jiang, X.-C. Lu, Numerical simulation of fluid flow and convection heat transfer in sintered porous plate channels, *Int. J. Heat Mass Transf.* 49 (9–10) (2006) 1685–1695.
- [66] J. Feng, H. Dong, J. Gao, J. Liu, K. Liang, Experimental study of gas–solid overall heat transfer coefficient in vertical tank for sinter waste heat recovery, *Appl. Therm. Eng.* 95 (2016) 136–142.
- [67] R. Pešić, T. Kaluderović Radoičić, N. Bošković-Vragolović, Z. Arsenijević, Ž. Grbavčić, Heat transfer between a packed bed and a larger immersed spherical particle, *Int. J. Heat Mass Transf.* 78 (2014) 130–136.
- [68] J. Shent, S. Kagueli, N. Wakao, Measurements of particle-to-gas heat transfer coefficients from one-shot thermal responses in packed beds, *Chem. Eng. Sci.* 36 (8) (1981) 1283–1286.
- [69] M. Al-Hasan, M.Q. Al-Odat, M. Al-Busoul, An experimental investigation of forced convection heat transfer from a coiled heat exchanger embedded in a packed bed, *Exp. Heat Transfer* 25 (4) (2012) 363–376.
- [70] L.B. Younis, R. Viskanta, Experimental determination of the volumetric heat transfer coefficient between stream of air and ceramic foam, *Int. J. Heat Mass Transf.* 36 (6) (1993) 1425–1434.
- [71] X. Fu, R. Viskanta, J.P. Gore, Measurement and correlation of volumetric heat transfer coefficients of cellular ceramics, *Exp. Therm. Fluid Sci.* 17 (4) (1998) 285–293.
- [72] Z. Wu, C. Caliot, G. Flamant, Z. Wang, Numerical simulation of convective heat transfer between air flow and ceramic foams to optimise volumetric solar air receiver performances, *Int. J. Heat Mass Transf.* 54 (7–8) (2011) 1527–1537.
- [73] K. Ando, H. Hirai, Y. Sano, An accurate experimental determination of interstitial heat transfer coefficients of ceramic foams using the single blow method, *Open Transport Phenom. J.* 5 (1) (2013) 7–12.
- [74] J.J. Hwang, G.J. Hwang, R.H. Yeh, C.H. Chao, Measurement of interstitial convective heat transfer and frictional drag for flow across metal foams, *J. Heat Transfer* 124 (1) (2001) 120–129.
- [75] A.G. Straatman, N.C. Gallego, B.E. Thompson, H. Hangan, Thermal characterization of porous carbon foam–convection in parallel flow, *Int. J. Heat Mass Transf.* 49 (11–12) (2006) 1991–1998.
- [76] D. Bhattacharyya, D.C.T. Pei, Heat transfer in fixed bed gas–solid systems, *Chem. Eng. Sci.* 30 (3) (1975) 293–300.
- [77] C.-H. Li, B.A. Finlayson, Heat transfer in packed beds—a reevaluation, *Chem. Eng. Sci.* 32 (9) (1977) 1055–1066.
- [78] N. Wakao, S. Kagueli, T. Funazkri, Effect of fluid dispersion coefficients on particle-to-fluid heat transfer coefficients in packed beds: correlation of nusselt numbers, *Chem. Eng. Sci.* 34 (3) (1979) 325–336.
- [79] A.G. Dixon, D.L. Cresswell, Theoretical prediction of effective heat transfer parameters in packed beds, *AIChE J.* 25 (4) (1979) 663–676.
- [80] E. Achenbach, Heat and flow characteristics of packed beds, *Exp. Thermal Fluid Sci.* 10 (1) (1995) 17–27.
- [81] K. Kamiuto, S.S. Yee, Heat transfer correlations for open-cellular porous materials, *Int. Commun. Heat Mass Transfer* 32 (7) (2005) 947–953.
- [82] M.S. Saidi, F. Rasouli, M.R. Hajaligol, Heat transfer coefficient for a packed bed of shredded materials at low peclet numbers, *Heat Transfer Eng.* 27 (7) (2006) 41–49.
- [83] A. Nakayama, K. Ando, C. Yang, Y. Sano, F. Kuwahara, J. Liu, A study on interstitial heat transfer in consolidated and unconsolidated porous media, *Heat Mass Transf.* 45 (11) (2009) 1365–1372.
- [84] N. Wakao, S. Kagueli, Heat and Mass Transfer in Packed Beds, Gordon and Breach Science Publishers, 1982.
- [85] S.E. Mahgoub, Forced convection heat transfer over a flat plate in a porous medium, *Ain Shams Eng. J.* 4 (4) (2013) 605–613.
- [86] P.-X. Jiang, B.-X. Wang, D.-A. Luo, Z.-P. Ren, Fluid flow and convective heat transfer in a vertical porous annulus, *Numer. Heat Transfer, Part A: Appl.* 30 (3) (1996) 305–320.
- [87] J. Chao, J. Lu, H. Yang, M. Zhang, Q. Liu, Experimental study on the heat transfer coefficient between a freely moving sphere and a fluidized bed of small particles, *Int. J. Heat Mass Transf.* 80 (2015) 115–125.
- [88] P.-X. Jiang, Z.-P. Ren, B.-X. Wang, Z. Wang, Forced convective heat transfer in a plate channel filled with solid particles, *J. Therm. Sci.* 5 (1) (1996) 43–53.
- [89] G.F. Al-Sumaily, A. Nakayama, J. Sheridan, M.C. Thompson, The effect of porous media particle size on forced convection from a circular cylinder without assuming local thermal equilibrium between phases, *Int. J. Heat Mass Transf.* 55 (13–14) (2012) 3366–3378.
- [90] Z.Y. Zhou, A.B. Yu, P. Zulli, Particle scale study of heat transfer in packed and bubbling fluidized beds, *AIChE J.* 55 (4) (2009) 868–884.
- [91] H. Roshan, M.O. Cuthbert, M.S. Andersen, R.I. Acworth, Local thermal non-equilibrium in sediments: implications for temperature dynamics and the use of heat as a tracer, *Adv. Water Resour.* 73 (2014) 176–184.
- [92] D. Kunii, J.M. Smith, Heat transfer characteristics of porous rocks: II. Thermal conductivities of unconsolidated particles with flowing fluids, *AIChE J.* 7 (1) (1961) 29–34.

- [93] M.S. Saidi, M.R. Hajjaligol, A. Mhaisekar, M. Subbiah, A 3D modeling of static and forward smoldering combustion in a packed bed of materials, *Appl. Math. Model.* 31 (9) (2007) 1970–1996.
- [94] G. Debenest, V.V. Mourzenko, J.F. Thovert, Three-dimensional microscale numerical simulation of smoldering process in heterogeneous porous media, *Combust. Sci. Technol.* 180 (12) (2008) 2170–2185.
- [95] I. Fabris, D. Cormier, J.I. Gerhard, T. Bartczak, M. Kortschot, J.L. Torero, Y.-L. Cheng, Continuous, self-sustaining smoldering destruction of simulated faeces, *Fuel* 190 (2017) 58–66.
- [96] L. Yermán, H. Wall, J. Torero, J. Gerhard, Y.L. Cheng, Smoldering combustion as a treatment technology for faeces: sensitivity to key parameters, *Combust. Sci. Technol.* (2016) null-null.
- [97] L. Yermán, D. Cormier, I. Fabris, J. Carrascal, J.L. Torero, J.I. Gerhard, Y.L. Cheng, Potential bio-oil production from smoldering combustion of faeces, *Waste Biomass Valor.* (2016) 1–10.
- [98] G. Baud, S. Salvador, G. Debenest, J.-F. Thovert, New granular model medium to investigate smoldering fronts propagation—experiments, *Energy Fuels* 29 (10) (2015) 6780–6792.
- [99] M. Sennoune, S. Salvador, M. Quintard, Toward the control of the smoldering front in the reaction-trailing mode in oil shale semicoke porous media, *Energy Fuels* 26 (6) (2012) 3357–3367.
- [100] M. Sennoune, S. Salvador, G. Debenest, Impact of a CO₂-enriched gas on the decarbonation of CaCO₃ and the oxidation of carbon in the smoldering process of oil shale semicoke, *Energy Fuels* 26 (1) (2012) 391–399.
- [101] M. Salman, J.I. Gerhard, D.W. Major, P. Pironi, R. Hadden, Remediation of trichloroethylene-contaminated soils by star technology using vegetable oil smoldering, *J. Hazard. Mater.* 285 (2015) 346–355.
- [102] P. Pironi, C. Switzer, J.I. Gerhard, G. Rein, J.L. Torero, Self-sustaining smoldering combustion for NAPL remediation: laboratory evaluation of process sensitivity to key parameters, *Environ. Sci. Technol.* 45 (7) (2011) 2980–2986.
- [103] L. Kinsman, J.L. Torero, J.I. Gerhard, Organic liquid mobility induced by smoldering remediation, *J. Hazard. Mater.* 325 (2017) 101–112.
- [104] A. D6539, Standard test method for measurement of pneumatic permeability of partially saturated porous materials by flowing air, in: ASTM International, West Conshohocken, PA, 2000, 2006.
- [105] S.E. Gustafsson, Transient plane source techniques for thermal conductivity and thermal diffusivity measurements of solid materials, *Rev. Sci. Instrum.* 62 (3) (1991) 797–804.
- [106] ASTM-E1269-11, Standard test method for determining specific heat capacity by differential scanning calorimetry, in: ASTM International, West Conshohocken, PA, 2011.
- [107] S. Lagüela, P. Bison, F. Peron, P. Romagnoni, Thermal conductivity measurements on wood materials with transient plane source technique, *Thermochim. Acta* 600 (2015) 45–51.
- [108] Y. Yang, T.G. Voskuilen, T.L. Pourpoint, D.R. Guildenbecher, J.P. Gore, Determination of the thermal transport properties of ammonia borane and its thermolysis product (polyiminoborane) using the transient plane source technique, *Int. J. Hydrogen Energy* 37 (6) (2012) 5128–5136.
- [109] T. Log, S.E. Gustafsson, Transient plane source (TPS) technique for measuring thermal transport properties of building materials, *Fire Mater.* 19 (1) (1995) 43–49.
- [110] A. Bejan, *Mass Transfer, Convection Heat Transfer*, John Wiley & Sons, Incorporated, 1995.
- [111] H. Darcy, Les fontaines publiques de la ville de Dijon: Exposition et application des principes à suivre et des formules à employer dans les questions de distribution d'eau; ouvrage terminé par un appendice relatif aux fournitures d'eau de plusieurs villes au filtrage des eaux et à la fabrication des tuyaux de fonte, de plomb, de toile et de bitume. Atlas, Victor Dalmont, Librairie des Corps impériaux des ponts et chaussées et des mines, 1856.
- [112] É. Clapeyron, Mémoire sur la puissance motrice de la chaleur, Jacques Gabay, 1834.
- [113] S. Rosseland, *Astrophysik und Atom-Theoretische Grundlagen*, Springer, Berlin, 1931.
- [114] F.P. Incropera, *Fundamentals of Heat and Mass Transfer*, John Wiley, 2007.
- [115] D.W. Marquardt, An algorithm for least square estimation of nonlinear parameters, *J. Soc. Ind. Appl. Math.* 11 (2) (1963) 431–441.
- [116] K. Levenberg, A method for the solution of certain non-linear problems in least square, *Q. Appl. Math.* 2 (2) (1944) 164–168.
- [117] M.N. Özisik, H.R.B. Orlande, *Inverse Heat Transfer*, 2000, pp. 35–114.
- [118] M.A. Bazelatto Zaroni, H. Massard, M. Ferreira Martins, Formulating and optimizing a combustion pathways for oil shale and its semi-coke, *Combust. Flame* 159 (10) (2012) 3224–3234.
- [119] M.A.B. Zaroni, H. Massard, M.F. Martins, S. Salvador, Application of inverse problem and thermogravimetry to determine the kinetics of oil shale pyrolysis, *High Temp. - High Press.* 41 (3) (2012) 197–213.
- [120] A. Bejan, K.R. Khair, Heat and mass transfer by natural convection in a porous medium, *Int. J. Heat Mass Transf.* 28 (5) (1985) 909–918.